

1 **Finite frequency inversion of cross-correlation**
2 **amplitudes for ambient noise source directivity**
3 **estimation**

4 **Arjun Datta¹, Shravan Hanasoge¹, and Jeroen Goudswaard²**

5 ¹Department of Astronomy and Astrophysics, Tata Institute of Fundamental Research, Homi Bhabha
6 Road, Colaba, Mumbai 400005, India.

7 ²Shell India Markets Private Limited, Devanahalli Industrial Park, Mahadeva Kodigehalli, Bangalore 562
8 149, Karnataka, India.

9 **Key Points:**

- 10 • Seismic noise directivity estimation by waveform inversion of noise correlations
11 • Applied to an exploration scale data set
12 • Observational uncertainties incorporated in inversion for source distribution

Corresponding author: A. Datta, arjun.datta@tifr.res.in

Abstract

We present a new method for determining the azimuthal variation of ambient noise sources, that combines the computational speed and simplicity of traditional approaches with the rigour of waveform-inversion-based approaches to noise-source estimation. This method is based on a previously developed theoretical framework of sensitivity kernels for cross-correlation amplitudes. It performs a tomographic inversion for ambient noise sources on the Earth's surface and is suitable for small (local) scale studies. We apply the method to passive seismic data acquired in an exploration context, and account for azimuth-dependent uncertainties in observed cross-correlation amplitudes. Our inversion results correlate well with the azimuthal distribution of noise sources suggested by signal-to-noise ratio analysis of noise cross-correlation functions.

1 Introduction

The issue of heterogeneous noise sources or noise directivity has received significant attention in the field of ambient-noise seismology. Several studies have reported inaccuracies or limitations associated with the seismic measurements that can be extracted from noise cross-correlation functions (NCFs), such as surface wave dispersion (Pedersen & Krüger, 2007; Tsai, 2009; Yao & van der Hilst, 2009; Kimman & Trampert, 2010; Froment et al., 2010; Wang et al., 2016) or anelastic attenuation (Tsai, 2011). Considerable effort has gone into developing tools for the proper exploitation of ambient-noise observations that are recognized to arise from anisotropically distributed sources (Roux, 2009; Curtis & Halliday, 2010; Wang et al., 2016). Knowledge of the sources of ambient-field measurements, particularly their spatial and/or temporal variations, is now widely recognized as a prerequisite to any attempts to use these measurements to study Earth structure (e.g. Delaney et al., 2017; Lehujeur et al., 2017).

The methods by which this information is typically obtained, with varying degrees of detail, fall under three broad categories: traditional array-processing or beamforming methods (e.g. Friedrich et al., 1998; Roux et al., 2005; Gerstoft & Tanimoto, 2007; Ruigrok et al., 2011; Gal et al., 2014; Nakata et al., 2015; Liu et al., 2016; Lörer et al., 2018), analysis of NCF asymmetry (Stehly et al., 2006; Yang & Ritzwoller, 2008; Ermert et al., 2016) and more recently, inversions for ambient-noise sources (Delaney et al., 2017; Ermert et al., 2017; Lehujeur et al., 2017). Inversions, by virtue of modelling and fitting

44 waveforms (or attributes thereof) are the most rigorous, especially when based on spa-
45 tially extended finite-frequency kernels.

46 The method we present in this paper carves a niche in this third category. Based
47 on acoustic modelling and inverting only for noise-source directions, it is free of the need
48 for expensive numerical simulations (Ermert et al., 2017) or ray-theoretical simplifica-
49 tions (Delaney et al., 2017). To the best of our knowledge it is also the first method to
50 demonstrably account for uncertainties in observed NCF amplitudes. The simplifications
51 of the method are that it is in 2-D (all sources and receivers required to be located on
52 a plane) and structural variations remain unmodelled (a uniform wavespeed is assumed).
53 At scales where the Earth’s sphericity may be neglected, the former condition is not lim-
54 iting because terrestrial seismic noise is known to be generated primarily on the Earth’s
55 surface (e.g. Webb, 1998). The latter restriction is also not a major impediment as am-
56 plitudes are used rather than traveltimes, so observed and synthetic waveforms can be
57 reconciled by a judicious choice of measurement. However the restrictions do imply that
58 our method is suitable for local-scale studies, not regional or continental scales (here the
59 term local-scale refers to length scales that are short enough for the Earth’s sphericity
60 to be negligible). As emphasized by Lehujeur et al. (2017), local-scale studies are im-
61 portant candidates for noise directivity analysis, because small-aperture networks likely
62 contain a significant fraction of measurements from interstation paths that are short com-
63 pared to the seismic wavelength — measurements for which the effects of anisotropic noise
64 sources are most pronounced (Bensen et al., 2007; Tsai, 2009; Froment et al., 2010).

65 We apply our method to an exploration-scale dataset acquired by Shell, which has
66 captured azimuthally varying ambient seismic noise over a period of several months. The
67 aim of this paper is method validation, not thorough characterization of our passive seis-
68 mic data set, so we limit this study to a single frequency band. Applying the method
69 to narrow frequency bands mitigates effects arising from neglecting (surface-wave) dis-
70 persion in the forward modelling. Our results are compared to those from NCF-asymmetry
71 analyses.

72 **2 Data and preliminary analysis**

73 Our data consist of one week (6-12 Nov 2016) of continuous ambient-field record-
74 ings taken by a network of 289 three-component, 5 Hz geophones placed over an area

75 $\sim 24 \text{ km} \times 28 \text{ km}$ (Figure 1). The data, stored in consecutive 10-minute intervals, have
 76 been downsampled from 4 ms to 20 ms sampling interval. For each 10-min window, vertical-
 77 component NCFs of 50 s duration are computed following standard processing techniques
 78 (Bensen et al., 2007), including running absolute-mean normalization and spectral whiten-
 79 ing after filtering the raw data in the frequency band 0.1–0.5 Hz. The results are then
 80 averaged over a 24-hour period to obtain NCFs for each day. Clear travelling waves are
 81 observed in record sections of the NCFs (Figure A.1).

82 We first attempt to characterize azimuthal variations in the strength of the daily
 83 NCFs. This is a type of NCF-asymmetry analysis that requires normalizing for differ-
 84 ent interstation distances (in each azimuth bin), since NCF amplitudes are expected to
 85 decay with distance (Cupillard & Capdeville, 2010). Ignoring the effects of anelastic at-
 86 tenuation, one way to perform this normalization is to multiply observed amplitudes by
 87 the inter-receiver distance (e.g. Stehly et al., 2006). This formalism rests on the implicit
 88 assumption that the data exhibit the canonical geometrical spreading rate of surface waves
 89 in a laterally homogeneous medium. We test this assumption in our data and find that
 90 there are many azimuths for which the observed NCF energies (E) are poorly described
 91 by the canonical decay rate. Sorting our daily NCFs into azimuth bins of 4° , regardless
 92 of absolute receiver location and inter-receiver distance r , we fit $1/r$ curves to the ob-
 93 served scatter in NCF energies plotted as a function of r (Figure A.2). Each NCF yields
 94 measurements for two (radially opposite) directions, because energies in the positive and
 95 negative branches of the waveform are measured separately. Figure 2 shows a polar plot
 96 of the χ^2 misfit comprising deviations from the $1/r$ approximation, for each azimuth bin.
 97 Given the significant deviations from theory at some azimuths, we infer that a normal-
 98 ization such as that of Stehly et al. (2006) would produce biases and lead to erroneous
 99 interpretation of dominant source directions. The method we propose in this paper is
 100 free of this potential bias because it does not require presuming an amplitude decay rate,
 101 but instead uses the observed amplitudes to quantify data errors in an inverse problem.

102 **3 Methodology and synthetic tests**

103 Hanasoge (2013) introduced sensitivity kernels for NCF amplitudes based on an-
 104 alytical solutions to an acoustic-wave equation in homogeneous 2-D media. In this method
 105 NCFs are forward modelled using a power spectrum $P(\omega)$ of spatially uncorrelated sources
 106 and their spatial-amplitude distribution $s(\mathbf{x})$ in a 2-D plane, along with a homogeneous

107 wavespeed. For the inverse problem, the method takes as input the NCF energy in a time
 108 window of interest (denoted by A), either on the positive or the negative branch, and
 109 computes source-amplitude kernels which define the sensitivity of this measurement to
 110 $s(\mathbf{x})$. Given a network of receivers, the method lends itself to a fast Hessian-based to-
 111 mographic inversion for source distribution. A misfit functional is defined which penal-
 112 izes the logarithmic ratio of A^{obs} of A^{syn} for all receiver pairs, and a misfit kernel K is
 113 obtained as the sum of individual source-amplitude kernels weighted by their misfits. Ex-
 114 cept for details of the measurement and misfit, this is analogous to, for instance, clas-
 115 sical (earthquake-based) finite frequency travelttime tomography with banana-doughnut
 116 kernels (e.g. Dahlen et al., 2000).

117 Hanasoge (2013) used synthetic tests to show the suitability of the misfit kernels
 118 for tomographic inversion. In this study, we take the straightforward next step of actu-
 119 ally performing these inversions. We choose a $100 \text{ km} \times 100 \text{ km}$ modelling domain with
 120 a uniform grid spacing of 0.25 km and a uniform wavespeed of 2.1 km/s , ensuring a sam-
 121 pling of 16 grid points per shortest wavelength ($\approx 4.4 \text{ km}$). The chosen wavespeed is
 122 estimated from the real data by picking the maxima of envelopes on NCF record sections
 123 (e.g. Figure S1) and averaging positive and negative branch values. Since we work with
 124 amplitudes, there is a trade off between the strength of sources and their distances from
 125 the receiver network, which we do not endeavour to resolve. We aim only to constrain
 126 the relative azimuthal distribution of noise sources. To this end, we parameterize our spa-
 127 tial source distribution as a ring of sources surrounding the network (see Figure 3a). The
 128 ring comprises M spatial Gaussians centered every 10° , which form a basis set for model
 129 expansion (see Supplement), and its radius must be sufficiently larger than the size of
 130 the network. In this paper we present results for a 50 km -wide ring but have verified with
 131 synthetic tests as well as real data, that the size of the ring has a negligible impact on
 132 the inferred source directions as long as the ring is wider than the array aperture. The
 133 model vector, of length M , simply contains the basis-function coefficients. We choose
 134 $M = 36$, thereby working with a highly tractable 36-parameter model space. Since in-
 135 dividual kernels for each receiver pair are computed, the gradient and Hessian of the mis-
 136 fit are both available, allowing us to invert using a standard quasi-Newton scheme (see
 137 Appendix B). The model update is obtained separately for positive- and negative-branch
 138 measurements and the two results are averaged. Our inverse method is validated by sev-
 139 eral synthetic tests, performed using the same network configuration as the real dataset.

140 We begin by using a test model that follows the parameterization used for the inverse
 141 problem (Figure 3), so all sources are constrained to lie on the same ring around the re-
 142 ceiver network. We run a series of examples using different-size subsets of the complete
 143 receiver network and the two end-member cases are shown in Figure 3. The combina-
 144 tion of misfit kernels from positive- and negative-branch measurements illuminates all
 145 model perturbations and the inversion recovers the true model with an accuracy that
 146 improves, as expected, with increased network coverage. With 256 receivers, the test re-
 147 sults are essentially perfect — all source locations and amplitudes are recovered exactly.
 148 Next, we employ a test model (Figure 4) that is free of the aforementioned parameter-
 149 ization, i.e. it contains arbitrarily oriented sources at arbitrary distances from the re-
 150 ceiver network. In this case it is difficult to quantify the accuracy of the model obtained
 151 by inversion (true source amplitude information is lost), but we argue that source direc-
 152 tions and their relative strengths are recovered reasonably well. Taken together, results
 153 from these tests validate the inverse algorithm and the imaging concept advocated by
 154 this paper. In particular, the latter tests justify our choice of 50 km for the size of the
 155 ring with which we parameterize the model space.

156 **4 Application to real data**

157 We apply the method to our data after tapering and downsampling the observed
 158 NCFs to 0.2 s. This factor-of-10 downsampling is in accord with the highest frequency
 159 considered (0.5 Hz) and reduces the computational cost of forward modelling. Based on
 160 the work of Section 3, the modified NCFs are subjected to inversion using a 60 km \times
 161 60 km modelling domain and 256 receivers. However three important considerations re-
 162 main: the choice of $P(\omega)$ for the noise sources, the choice of window size for the mea-
 163 surements A , and quantification of observational errors or uncertainties. We discuss each
 164 one in detail.

165 A judicious choice of $P(\omega)$ is required to produce synthetic NCFs that match the
 166 input observed NCFs not only in shape (frequency content) but also – in order to ini-
 167 tialize the inversion – in order of magnitude of amplitude. Since $P(\omega)$ contributes to the
 168 synthetic NCFs through interaction with other terms in a spatial integral (Hanasoge, 2013,
 169 eq. 11), it is empirically estimated as a skew-symmetric Gaussian function (Figure A.3a).
 170 Its amplitude is determined by requiring that the initial synthetics have energies equal
 171 to an average representation of the observed NCF energies, namely the $1/r$ curve that

172 best fits the observed NCF energies as a function of interstation distance (Figure A.3b).
 173 This is similar to the analysis of Section 2 but here, the energies are computed for com-
 174 plete NCFs (not separately for positive and negative branches) and all observations are
 175 taken together, regardless of azimuth. The second consideration, that of the measure-
 176 ment window, is important because the window needs to be narrow enough to ensure
 177 that it fits only the coherent signals in the NCFs and yet broad enough to accommodate
 178 those cases where the signals in the observed and synthetic NCFs are significantly off-
 179 set from each other in time (the chosen wavespeed is likely a poor approximation in some
 180 parts of the study region). We set an 8 s window around the central arrival time dictated
 181 by the chosen homogeneous wavespeed. The taper applied to the observed NCFs exists
 182 only outside and beyond this measurement window.

183 Lastly, the data analysis is made meaningful by introducing data errors into the
 184 inverse problem. We consider two types of error: σ_1 , based on the energy-decay anal-
 185 ysis of Section 2, and σ_2 , due to the signal-to-noise ratio (SNR) of the observed NCFs.
 186 The first error, σ_1 , is simply an estimate for ΔA obtained using $A = \sqrt{E}$, and ΔE as
 187 yielded by curve-fitting in the relevant azimuth bin (e.g. Figure S2). SNR is defined as
 188 the ratio of the energy density of an NCF in a time window of interest (we use the in-
 189 version measurement window), to its energy density outside that window. Similar to the
 190 analysis of Section 2, SNR is measured separately on the positive and negative branches,
 191 yielding two values for each NCF and therefore an error estimate (σ_2) for each measure-
 192 ment made for source inversion. SNR values are translated into data errors by qualita-
 193 tively identifying three SNR regimes (> 3 , $2 < \text{SNR} < 3$ and < 2) to which we as-
 194 sign $\sigma_2 = 5\%$, 50% and 80% respectively of the A value. We assume that errors on dif-
 195 ferent measurements are uncorrelated (\mathbf{C}_D in (B.12) is diagonal) and that the two er-
 196 rors considered are independent, i.e. $\sigma^2 = \sigma_1^2 + \sigma_2^2$. The latter assumption is based on
 197 the observation that high SNR values coincide with large departures from a $1/r$ energy
 198 decay rate (see Figures 2,6). Other sources of error, such as neglecting the topography
 199 of the region and differing station elevations, are not explicitly accounted for.

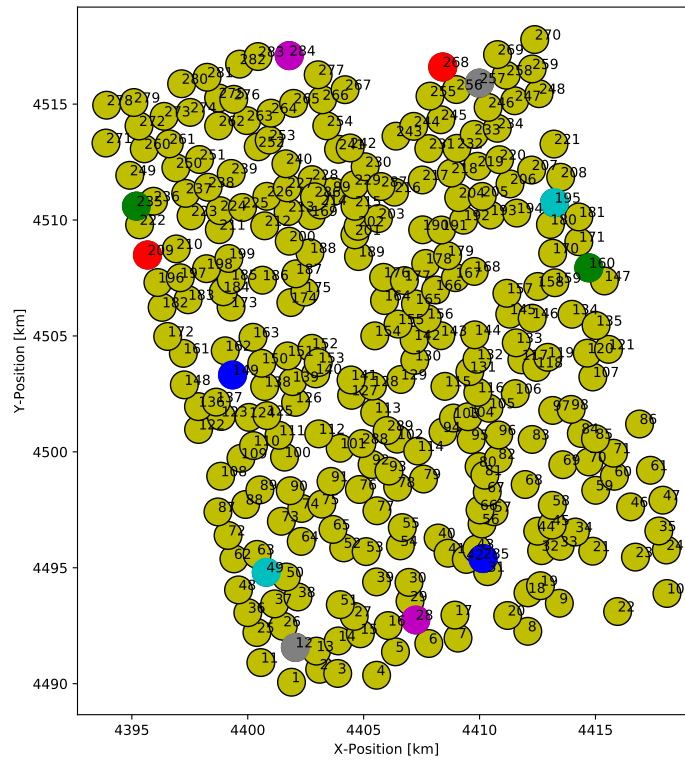
200 The inverse algorithm thus customized, is applied separately to the observed NCFs
 201 for each day. We achieve total misfit reductions of $\sim 70 - 80\%$, with at least 50% of
 202 measurements being fit to an accuracy greater than 70% . An example of this quantita-
 203 tive summary for one of the days is shown in Figure 5. Finally, we corroborate our re-
 204 sults with the simple idea of using SNR itself as a proxy for source directionality. Az-

205 imuthal polar plots of SNR are obtained in a manner similar to Figure 2, with the ex-
 206 ception that, here, distance does not play an explicit role – SNR values for different in-
 207 terstation distances within an azimuth bin are averaged. Yang & Ritzwoller (2008) used
 208 this kind of analysis on long-range correlations to infer noise-source directions at con-
 209 tinental scales. In this study, we find that subtle variations – on daily time scales – in
 210 the dominant wave-propagation directions (primarily between ENE and NNE) inferred
 211 from SNR polar plots, correlate well with variations in the azimuthal noise-source dis-
 212 tribution obtained by our inverse method (Figure 6). Also, there is qualitative agreement
 213 between the two methods, on the apparent strength of noise sources on different days
 214 – SNR values are highest on days 3-5, as are source amplitudes obtained by inversion.

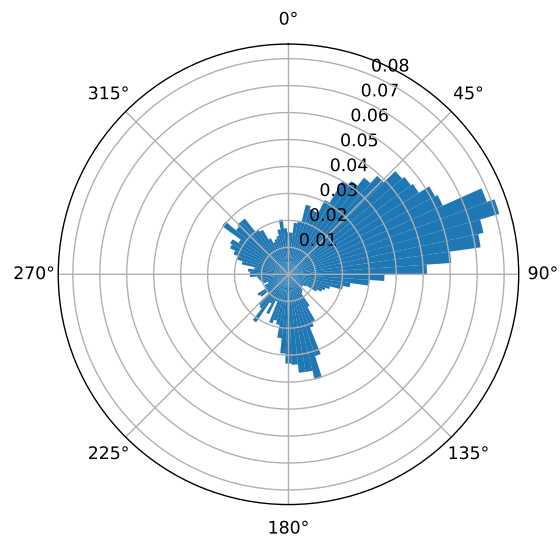
215 **5 Discussion and conclusions**

216 We have introduced a new method of determining ambient noise-source direction-
 217 ality by inverting NCF amplitudes. In its present form, the method is suitable for local-
 218 scale studies, where the effects of Earth’s sphericity are negligible. The main attraction
 219 of the technique compared to existing approaches is the combination of computational
 220 ease and rigorous waveform-fitting. Although the method owes its economy to strong sim-
 221 plifying approximations, these do not preclude its application. In particular, the use of
 222 amplitudes ensures that Earth structure has a diminished impact on the measurements.
 223 We applied the technique to a study region with known strong lateral variations in ge-
 224 ological structure, and achieved waveform fits comparable with typical seismic tomog-
 225 raphy applications.

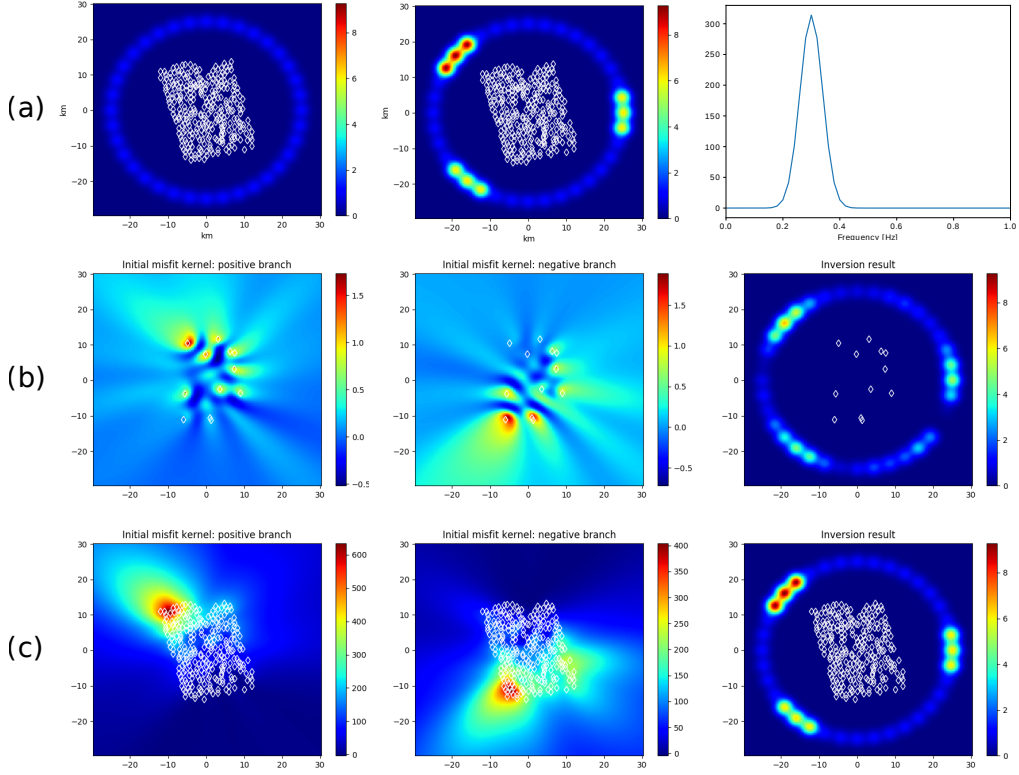
226 The real data application systematically accounts for observational uncertainties,
 227 and demonstrates the suitability of the method for studying non-stationarity in ambient-
 228 noise-source distributions over short timescales (e.g. hours or days for reservoir moni-
 229 toring). This is possible because the technique may be applied to ambient seismic noise
 230 of shorter duration than is typically used in most applications. In this respect, it con-
 231 tributes to a growing body of seismological research (e.g. Roux & Ben-Zion, 2017; Ficht-
 232 ner et al., 2017) that treats NCFs as fundamental seismic observables in their own right,
 233 without the requirement of convergence to an interstation Green’s function.



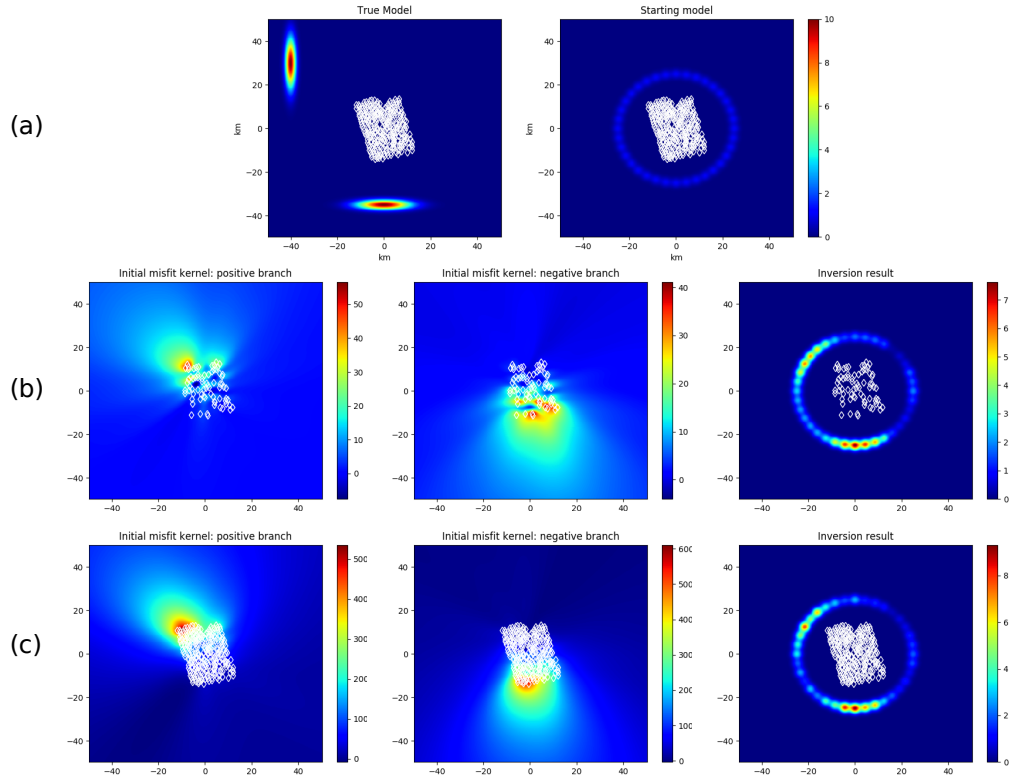
234 **Figure 1.** Map view of network of recording geophones, numbered from 1 to 289. Colours
 235 other than yellow indicate six receiver pairs selected for later reference in Figure 5.



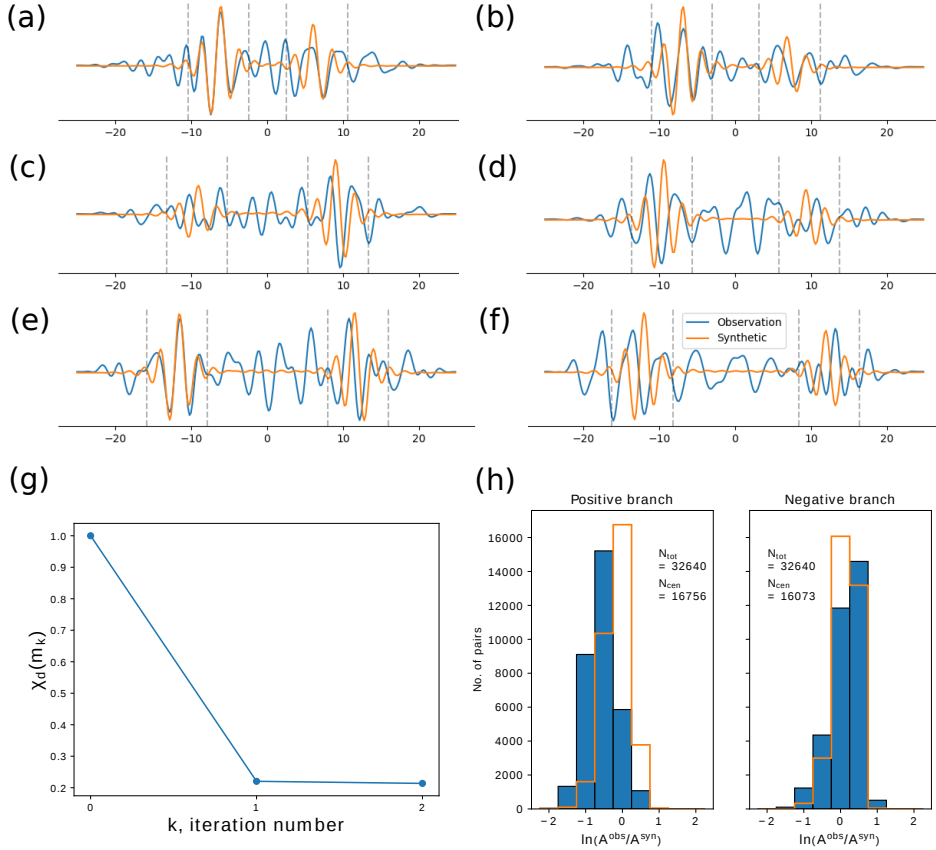
236 **Figure 2.** Single-day example (day 3) of azimuthal variation in the departure of the observed
 237 cross-correlation energies from a $1/r$ energy decay regime, where r is interstation distance. Plot-
 238 ted values are the χ^2 misfit obtained in each azimuth bin – refer to text and Figure A.2.



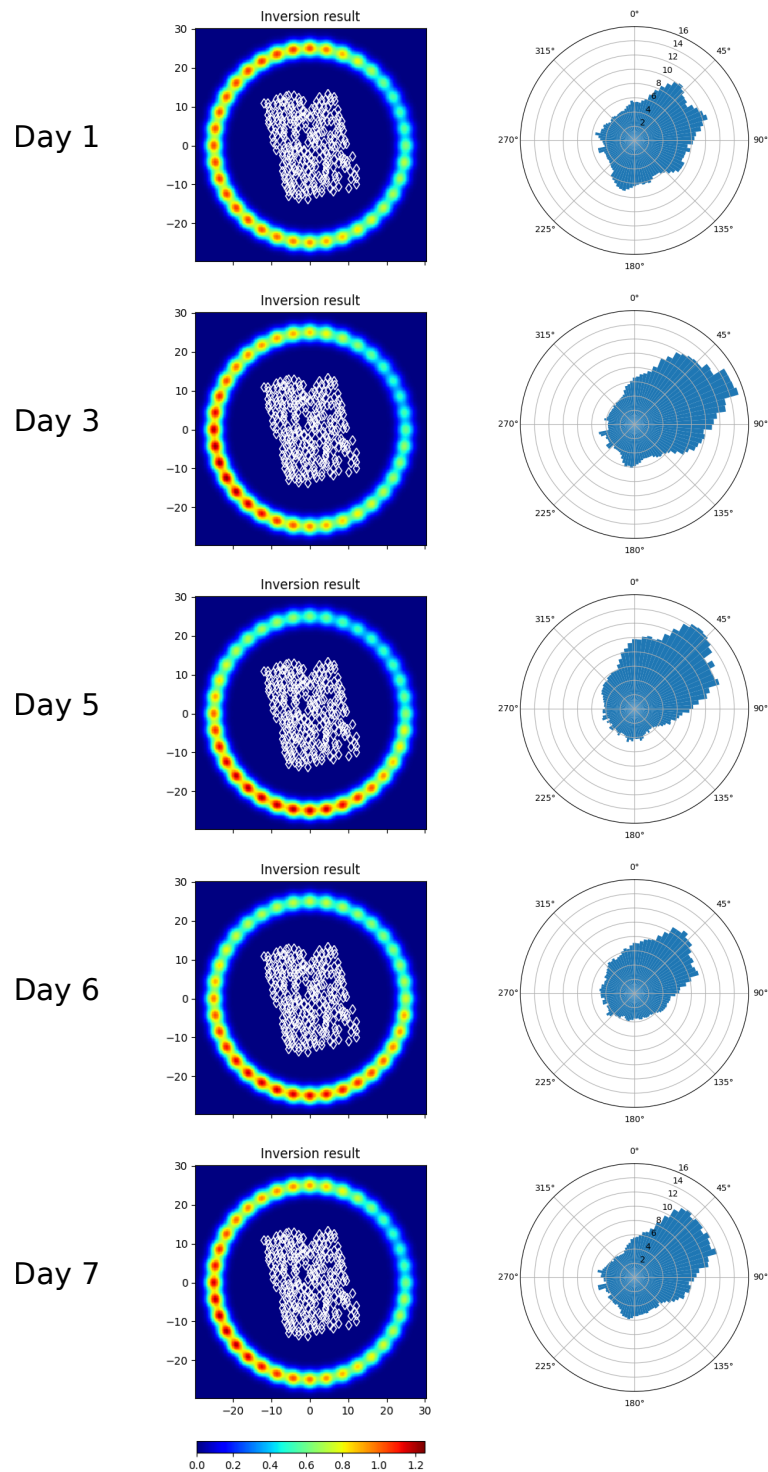
239 **Figure 3.** Type 1 synthetic test of the inverse method. (a) Left: Reference model with an
 240 azimuthally homogeneous $s(\mathbf{x})$ shown in colour. All basis functions have unit amplitude in this
 241 model and it serves as the starting model for inversions. Middle: The “true model” for the
 242 synthetic test, comprising three high-amplitude regions relative to the reference model. Right:
 243 Assumed $P(\omega)$ for the sources, centred at 0.3 Hz. (b) Inversion performed using only 12 receivers:
 244 starting misfit kernels for the positive- (left panel) and negative-branch (middle panel) measure-
 245 ments, and the inversion result after 8 iterations (right panel). (c) Same as (b) but with 256
 246 receivers. Note that all the model plots have the same colour scale and in all plots, the white
 247 diamonds mark the receiver locations.



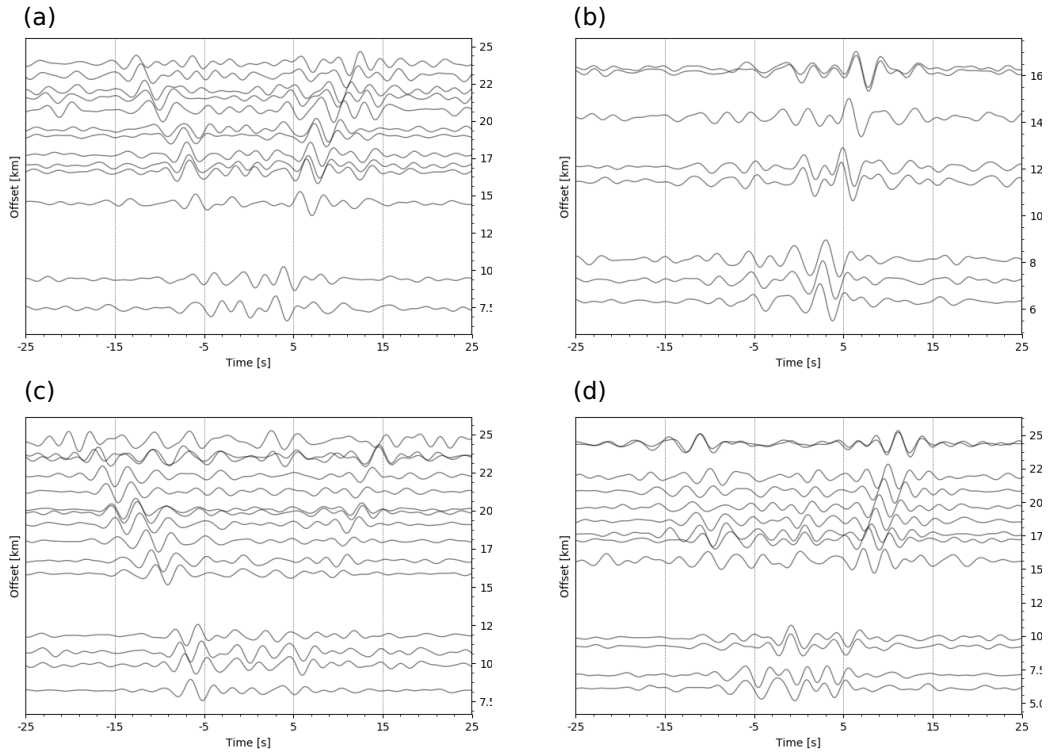
248 **Figure 4.** Type 2 synthetic test. (a) True model (left) and starting model for inversions
 249 (right, same as in Figure 3). In the true model, the high amplitude regions to the North West
 250 and South of the receiver network are at distances of 50 km and 35 km respectively, from the
 251 network centre. (b)-(c) same as in Figure 3 except that (b) uses 72 receivers. Note that both
 252 inversions predict higher source amplitudes South of the receiver network than North West of it –
 253 commensurate with the sources in the true model being closer to the network in the South than
 254 in the North West.



255 **Figure 5.** Summary of inversion for day 3. (a)-(f) Six examples of waveform fits after in-
 256 version; these correspond to receiver pairs highlighted in blue (285-149), red (268-209), green
 257 (235-160), cyan (195-49), magenta (284-28) and grey (257-12) respectively, in Figure 1. All plots
 258 share the same legend and the vertical black dashed lines represent the 8-s measurement window
 259 in each case. Note that (e) has the greatest symmetry in amplitude between the positive and
 260 negative branches, and it corresponds to a receiver pair that is oriented approximately transverse
 261 to the dominant incoming energy direction (see Figure 6). (d) Evolution of the total data misfit
 262 χ_d (normalized for plotting) through the inversion, showing a misfit reduction of nearly 80% (e)
 263 Histograms of Δd values from all interstation pairs in the starting model (blue filled bars) and in
 264 the final inverted model (orange step bars). Note that data errors are included in χ_d but not in
 265 Δd . Text on the plots indicates the total number of measurements (N_{tot}) and those that lie in
 266 the central histogram bin after inversion (N_{cen}). The central bin corresponds to $|\Delta d| \leq 0.25$, or
 267 a maximum waveform discrepancy (as defined by the measurement) of about 28%. In this case,
 268 32829 measurements (out of the total 65280) lie in the central bin after inversion, meaning that
 269 $\sim 50.3\%$ of total measurements are fit to an accuracy of at least 72%.

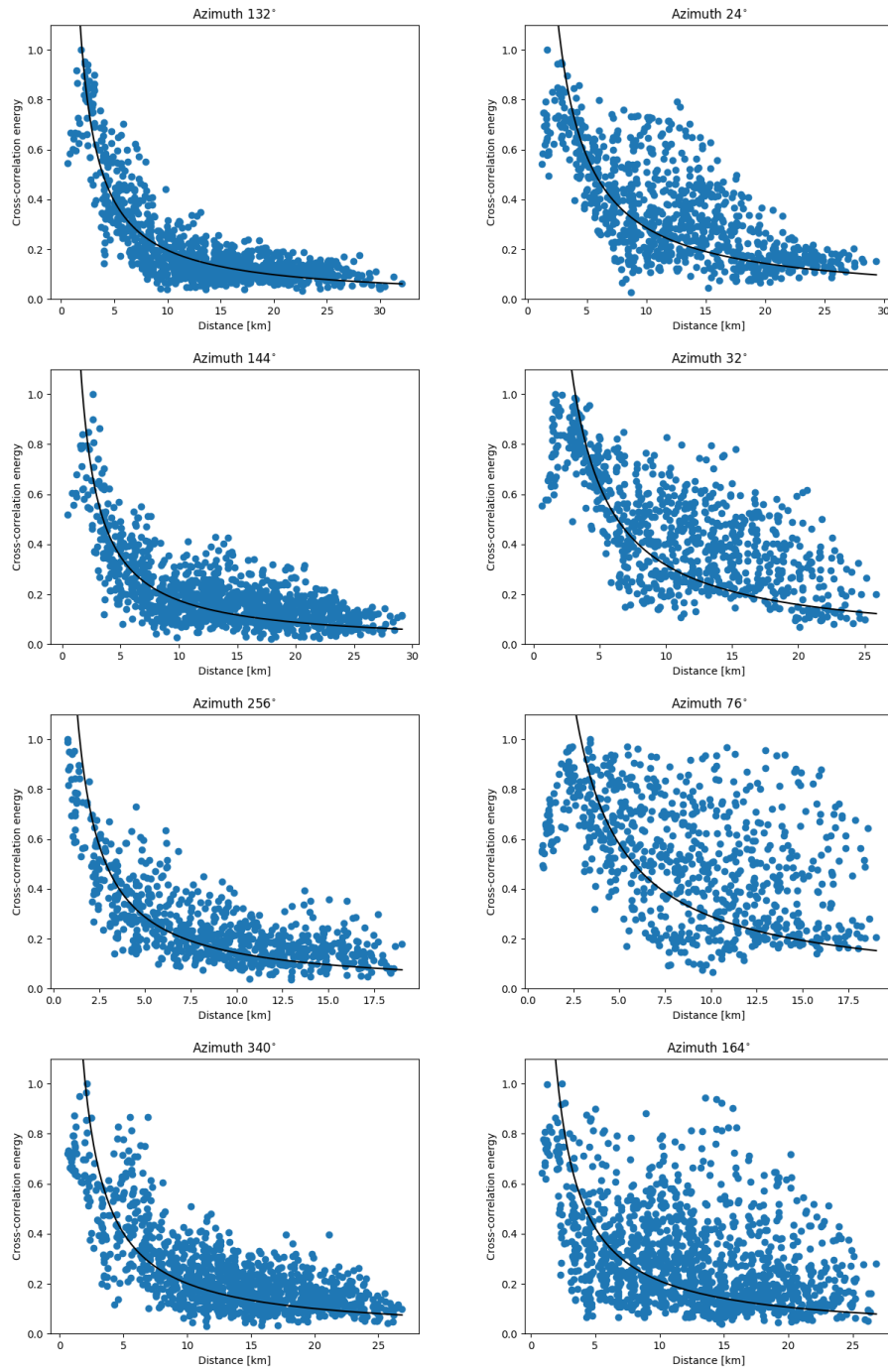


270 **Figure 6.** Results corresponding to different days of data from our method (left column) and
 271 from SNR analysis (right column). In the SNR plots, each bar points in the direction of wave
 272 propagation, i.e. it points away from the source location.

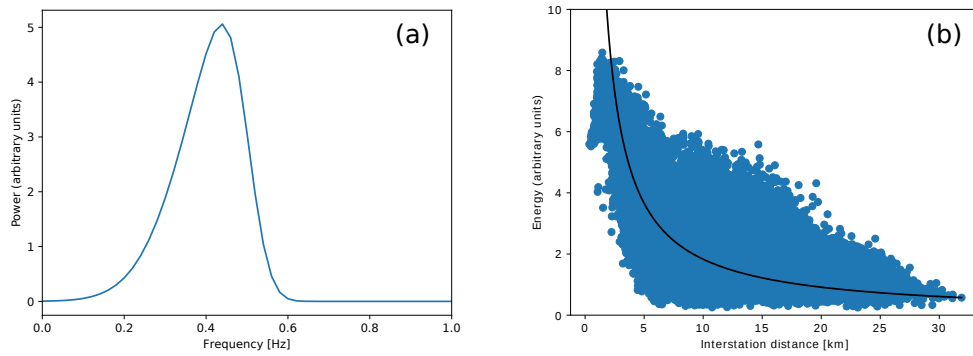


274 **Figure A.1.** Examples of record sections of NCFs obtained from one day of data, correspond-
 275 ing to a single base receiver (number 29) and azimuths of (a) 10° (b) 30° (c) 332° and (d) 344°
 276 with respect to North. Note that relative amplitudes are not represented in these plots because
 277 each plot contains independent normalization for each waveform.

273 **A Supporting figures**



278 **Figure A.2.** Normalized observed NCF energies (blue circles) and the best-fit $1/r$ curve,
 279 as a function of interstation distance r . Shown are plots for 8 randomly selected azimuth bins,
 280 qualitatively separated into “good” (left) and “bad” (right) fits. Corresponds to Figure 2 of main
 281 paper.



282 **Figure A.3.** (a) Shape of $P(\omega)$ used for real data inversions. (b) Azimuth-independent,
 283 complete-NCF energy fitting used to initialize said inversions. The starting synthetics for inver-
 284 sion have energies given by the black curve. The curve and symbols have the same meaning as in
 285 Figure A.2.

286 **B Model parameterization and inversion**

287 Equation (28) of Hanasoge (2013) may be written as:

$$\delta\chi = - \int K(\mathbf{x})\delta s(\mathbf{x})d^2\mathbf{x} \quad (\text{B.1})$$

where $s(\mathbf{x})$ is the spatial source distribution, $K(\mathbf{x})$ the misfit kernel and χ the misfit functional defined as:

$$\begin{aligned} \chi &= \frac{1}{2} \sum_i \left(\ln \frac{A_i^{obs}}{A_i^{syn}} \right)^2 \\ &= \frac{1}{2} [\mathbf{d}_{obs} - \mathbf{d}_{syn}]^T [\mathbf{d}_{obs} - \mathbf{d}_{syn}] \end{aligned} \quad (\text{B.2})$$

with index i denoting the i^{th} receiver-receiver pair. Expanding the model perturbation into the model-space basis functions B_j , we have

$$\delta s(\mathbf{x}) = \sum_{j=1}^M \delta m_j B_j(\mathbf{x}) \quad (\text{B.3})$$

Using (B.3) in (B.1) gives

$$\delta\chi = \sum_{j=1}^M \left[- \int K(\mathbf{x})B_j(\mathbf{x})d^2\mathbf{x} \right] \delta m_j \quad (\text{B.4})$$

from which it is clear that the quantity in square brackets represents the gradient (\mathbf{g}) of χ :

$$\frac{\partial\chi}{\partial m_j} = - \int K(\mathbf{x})B_j(\mathbf{x})d^2\mathbf{x} = g_j \quad (\text{B.5})$$

288 To express the gradient in terms of the customary \mathbf{G} matrix that linearizes the in-
 289 verse problem, we need only invoke the fact that the misfit kernel is a weighted sum of
 290 source kernels for individual receiver pairs (Hanasoge, 2013, eq. 30):

$$K = \sum_i \ln \left(\frac{A_i^{obs}}{A_i^{syn}} \right) K_i(\mathbf{x}) \quad (\text{B.6})$$

Using (B.6) in (B.5), we have

$$\begin{aligned} g_j &= - \sum_i \ln \left(\frac{A_i^{obs}}{A_i^{syn}} \right) \int K_i(\mathbf{x})B_j(\mathbf{x})d^2\mathbf{x} \\ &= -G_{ij}\Delta d_i \end{aligned} \quad (\text{B.7})$$

or

$$\mathbf{g} = -\mathbf{G}^T \Delta \mathbf{d} \quad (\text{B.8})$$

where the \mathbf{G} matrix and $\Delta \mathbf{d}$ vector are given by:

$$\begin{aligned} G_{ij} &= \int K_i(\mathbf{x}) B_j(\mathbf{x}) d^2 \mathbf{x} \\ \Delta d_i &= \ln \left(\frac{A_i^{\text{obs}}}{A_i^{\text{syn}}} \right) \end{aligned} \quad (\text{B.9})$$

Using \mathbf{G} , the approximate Hessian \mathbf{H} for a Gauss-Newton inversion is easily computed:

$$\mathbf{H} = \mathbf{G}^T \mathbf{G} \quad (\text{B.10})$$

291 In practice, the canonical expressions (B.8) and (B.10) are modified, because the
 292 objective function itself is modified by damping (required to overcome solution under-
 293 determinacy) and weighting by model or data (co-)variances (required to control the ex-
 294 tent of damping or to incorporate observation errors, as in Section 4). The inverse prob-
 295 lem we actually work with is (e.g. Tarantola, 2005):

$$\begin{aligned} \tilde{\chi} &= \frac{1}{2} [\mathbf{d}_{\text{obs}} - \mathbf{d}_{\text{syn}}]^T \mathbf{C}_D^{-1} [\mathbf{d}_{\text{obs}} - \mathbf{d}_{\text{syn}}] + \frac{1}{2} [\mathbf{m} - \mathbf{m}_{\text{prior}}]^T \mathbf{C}_M^{-1} [\mathbf{m} - \mathbf{m}_{\text{prior}}] \\ &= \chi_d + \chi_m \\ \tilde{\mathbf{g}} &= -\mathbf{G}^T \mathbf{C}_D^{-1} \Delta \mathbf{d} - \mathbf{C}_M^{-1} (\mathbf{m} - \mathbf{m}_{\text{prior}}) \\ \tilde{\mathbf{H}} &= \mathbf{G}^T \mathbf{C}_D^{-1} \mathbf{G} + \mathbf{C}_M^{-1} \end{aligned} \quad (\text{B.11})$$

296 Here \mathbf{C}_D and \mathbf{C}_M are the model and data covariance matrices. We use $\mathbf{C}_D = \mathbf{I}$ and
 297 $\mathbf{C}_D(i, j) = \sigma_{ij}^2 \delta_{ij}$ in sections 3 and 4 respectively. Correspondingly, for \mathbf{C}_M we use $\mathbf{C}_M =$
 298 $\frac{1}{\gamma^2} \mathbf{I}$ and $\mathbf{C}_M(i, j) = \frac{1}{\gamma^2} \exp\left(\frac{-(i-j)^2}{2L^2}\right)$ respectively. Here γ is a damping parameter and
 299 L is a correlation length that controls the smoothness of the model; they are both de-
 300 termined empirically. These choices for \mathbf{C}_D and \mathbf{C}_M imply that the synthetic test in-
 301 versions are carried out with no data errors and no smoothing, whereas the real data in-
 302 versions are done with both errors and smoothing included.

Choosing $\mathbf{m}_{\text{prior}} = \mathbf{m}_0$ and applying the Gauss-Newton method $\tilde{\mathbf{H}} \Delta \mathbf{m} = -\tilde{\mathbf{g}}$
 to (B.11) leads to the following iterative solution:

$$\mathbf{m}_{k+1} = \mathbf{m}_k + [\mathbf{G}_k^T \mathbf{C}_D^{-1} \mathbf{G}_k + \mathbf{C}_M^{-1}]^{-1} [\mathbf{G}_k^T \mathbf{C}_D^{-1} \Delta \mathbf{d}_k + \mathbf{C}_M^{-1} (\mathbf{m}_k - \mathbf{m}_0)] \quad (\text{B.12})$$

303 where index k denotes the iteration number.

304 **Acknowledgments**

305 This work was funded by Shell India Markets Pvt. Ltd. Computing was performed on
 306 the SEISMO cluster at Tata Institute of Fundamental Research. The data used in this
 307 study are owned by Shell International Exploration and Production B.V., and can be
 308 obtained from them.

309 **References**

- 310 Bensen, G. D., Ritzwoller, M. H., Barmin, M. P., Levshin, A. L., Lin, F., Moschetti,
 311 M. P., . . . Yang, Y. (2007). Processing seismic ambient noise data to obtain reli-
 312 able broad-band surface wave dispersion measurements. *Geophys. J. Int.*, *169*(3),
 313 1239–1260. doi: 10.1111/j.1365-246X.2007.03374.x
- 314 Cupillard, P., & Capdeville, Y. (2010). On the amplitude of surface waves obtained
 315 by noise correlation and the capability to recover the attenuation: a numerical
 316 approach. *Geophys. J. Int.* doi: 10.1111/j.1365-246X.2010.04586.x
- 317 Curtis, A., & Halliday, D. (2010). Directional balancing for seismic and gen-
 318 eral wavefield interferometry. *GEOPHYSICS*, *75*(1), SA1–SA14. doi:
 319 10.1190/1.3298736
- 320 Dahlen, F. A., Hung, S.-H., & Nolet, G. (2000). Fréchet kernels for finite-frequency
 321 traveltimes-I. Theory. *Geophys. J. Int.*, *141*(1), 157–174. doi: 10.1046/j.1365-246X
 322 .2000.00070.x
- 323 Delaney, E., Ermert, L., Sager, K., Kritski, A., Bussat, S., & Fichtner, A. (2017).
 324 Passive seismic monitoring with nonstationary noise sources. *GEOPHYSICS*,
 325 *82*(4), KS57–KS70. doi: 10.1190/geo2016-0330.1
- 326 Ermert, L., Sager, K., Afanasiev, M., Boehm, C., & Fichtner, A. (2017). Ambi-
 327 ent Seismic Source Inversion in a Heterogeneous Earth: Theory and Application
 328 to the Earth’s Hum. *J. Geophys. Res. Solid Earth*, *122*(11), 9184–9207. doi:
 329 10.1002/2017JB014738
- 330 Ermert, L., Villaseñor, A., & Fichtner, A. (2016). Cross-correlation imaging of ambi-
 331 ent noise sources. *Geophys. J. Int.*, *204*(1), 347–364. doi: 10.1093/gji/ggv460
- 332 Fichtner, A., Stehly, L., Ermert, L., & Boehm, C. (2017). Generalized interferome-
 333 try I: theory for interstation correlations. *Geophys. J. Int.*, *208*(2), 603–638. doi:
 334 10.1093/gji/ggw420
- 335 Friedrich, A., Krüger, F., & Klinge, K. (1998). Ocean-generated microseismic noise

- 336 located with the Gräfenberg array. *J. Seismol.*, 2(1), 47–64. doi: 10.1023/A:
337 1009788904007
- 338 Froment, B., Campillo, M., Roux, P., Gouédard, P., Verdel, A., & Weaver, R. L.
339 (2010). Estimation of the effect of nonisotropically distributed energy on the
340 apparent arrival time in correlations. *GEOPHYSICS*, 75(5), SA85–SA93. doi:
341 10.1190/1.3483102
- 342 Gal, M., Reading, A. M., Ellingsen, S. P., Koper, K. D., Gibbons, S. J., & Näsholm,
343 S. P. (2014). Improved implementation of the fk and Capon methods for
344 array analysis of seismic noise. *Geophys. J. Int.*, 198(2), 1045–1054. doi:
345 10.1093/gji/ggu183
- 346 Gerstoft, P., & Tanimoto, T. (2007). A year of microseisms in southern California.
347 *Geophys. Res. Lett.*, 34(20), L20304. doi: 10.1029/2007GL031091
- 348 Hanasoge, S. M. (2013). The influence of noise sources on cross-correlation ampli-
349 tudes. *Geophys. J. Int.*, 192(1), 295–309. doi: 10.1093/gji/ggs015
- 350 Kimman, W. P., & Trampert, J. (2010). Approximations in seismic interferome-
351 try and their effects on surface waves. *Geophys. J. Int.*, 182(1), 461–476. doi: 10
352 .1111/j.1365-246X.2010.04632.x
- 353 Lehujeur, M., Vergne, J., Maggi, A., & Schmittbuhl, J. (2017). Ambient noise to-
354 mography with non-uniform noise sources and low aperture networks: case study
355 of deep geothermal reservoirs in northern Alsace, France. *Geophys. J. Int.*, 208(1),
356 193–210. doi: 10.1093/gji/ggw373
- 357 Liu, Q., Koper, K. D., Burlacu, R., Ni, S., Wang, F., Zou, C., . . . Reading, A. M.
358 (2016). Source locations of teleseismic P, SV, and SH waves observed in micro-
359 seisms recorded by a large aperture seismic array in China. *Earth Planet. Sci.*
360 *Lett.* doi: 10.1016/j.epsl.2016.05.035
- 361 Lörer, K., Riahi, N., & Saenger, E. H. (2018). Three-component ambient noise beam-
362 forming in the Parkfield area. *Geophys. J. Int.*, 213(3), 1478–1491. doi: 10.1093/
363 gji/ggy058
- 364 Nakata, N., Chang, J. P., Lawrence, J. F., & Boué, P. (2015). Body wave extraction
365 and tomography at Long Beach, California, with ambient-noise interferometry. *J.*
366 *Geophys. Res. Solid Earth*, 120(2), 1159–1173. doi: 10.1002/2015JB011870
- 367 Pedersen, H. A., & Krüger, F. (2007). Influence of the seismic noise characteristics
368 on noise correlations in the Baltic shield. *Geophys. J. Int.*, 168(1), 197–210. doi:

369 10.1111/j.1365-246X.2006.03177.x

370 Roux, P. (2009). Passive seismic imaging with directive ambient noise: application
 371 to surface waves and the San Andreas Fault in Parkfield, CA. *Geophys. J. Int.*,
 372 *179*(1), 367–373. doi: 10.1111/j.1365-246X.2009.04282.x

373 Roux, P., & Ben-Zion, Y. (2017). Rayleigh phase velocities in Southern California
 374 from beamforming short-duration ambient noise. *Geophys. J. Int.*, *211*(1), 450–
 375 454. doi: 10.1093/gji/ggx316

376 Roux, P., Sabra, K. G., Gerstoft, P., Kuperman, W. A., & Fehler, M. C. (2005). P-
 377 waves from cross-correlation of seismic noise. *Geophys. Res. Lett.*, *32*(19), L19303.
 378 doi: 10.1029/2005GL023803

379 Ruigrok, E., Campman, X., & Wapenaar, K. (2011). Extraction of P-wave reflec-
 380 tions from microseisms. *Comptes Rendus Geosci.*, *343*(8-9), 512–525. doi: 10
 381 .1016/J.CRTE.2011.02.006

382 Stehly, L., Campillo, M., & Shapiro, N. M. (2006). A study of the seismic noise from
 383 its long-range correlation properties. *J. Geophys. Res.*, *111*(B10), B10306. doi: 10
 384 .1029/2005JB004237

385 Tarantola, A. (2005). *Inverse Problem Theory and Methods for Model Parame-*
 386 *ter Estimation*. Society for Industrial and Applied Mathematics. doi: 10.1137/1
 387 .9780898717921

388 Tsai, V. C. (2009). On establishing the accuracy of noise tomography travel-time
 389 measurements in a realistic medium. *Geophys. J. Int.*, *178*(3), 1555–1564. doi: 10
 390 .1111/j.1365-246X.2009.04239.x

391 Tsai, V. C. (2011). Understanding the amplitudes of noise correlation measurements.
 392 *J. Geophys. Res.*, *116*(B9), B09311. doi: 10.1029/2011JB008483

393 Wang, K., Luo, Y., & Yang, Y. (2016). Correction of phase velocity bias caused
 394 by strong directional noise sources in high-frequency ambient noise tomogra-
 395 phy: a case study in Karamay, China. *Geophys. J. Int.*, *205*(2), 715–727. doi:
 396 10.1093/gji/ggw039

397 Webb, S. C. (1998). Broadband seismology and noise under the ocean. *Rev. Geo-*
 398 *phys.*, *36*(1), 105–142. doi: 10.1029/97RG02287

399 Yang, Y., & Ritzwoller, M. H. (2008). Characteristics of ambient seismic noise as
 400 a source for surface wave tomography. *Geochemistry, Geophys. Geosystems*, *9*(2),
 401 Q02008. doi: 10.1029/2007GC001814

402 Yao, H., & van der Hilst, R. D. (2009). Analysis of ambient noise energy distribution
403 and phase velocity bias in ambient noise tomography, with application to SE Ti-
404 bet. *Geophys. J. Int.*, *179*(2), 1113–1132. doi: 10.1111/j.1365-246X.2009.04329.x